scientific reports

Check for updates

OPEN

Multi-GeV electron beam generation via two-stage laser wakefield acceleration

Rashid Ul Haq[1,2], Mohammad Rezaei-Pandari[3], Xinglong Xie[1,2]✉, Xiao Liang[1]✉, Meizhi Sun[1], Ping Zhu[1], Zhantao Lu[1,2], Guoli Zhang[1,2], Linjun Li[1,2], Hao Xue[1,2], Nasr A. M. Hafz[1,4] & Jianqiang Zhu[1,2]

Despite considerable progress in multi-stage laser wakefield acceleration (MSLWFA), efficient coupling between stages and the impact of laser–beam injection delay remains open challenges. A two-stage LWFA scheme is demonstrated using particle-in-cell (PIC) simulations, capable of producing multi-GeV electron beams over millimeter-scale propagation lengths. In the first stage, a high-intensity laser pulse (with $a_0 = 7.7,\ w_0 = 20\mu\, m,\ \tau\ = 30\ fs,\ E = 30\ J,\ \lambda_0$ = 800 nm and $I_0 = 1.2\ \times\ 10^{20}\ W/cm^2$) propagates through a neutral helium (He) gas target inside a gas cell, with ionization modeled self-consistently to produce a fully ionized plasma at a plateau density $7\ \times\ 10^{18}\ cm^{-3}$, generating a high-quality 1 GeV electron beam. This beam is then injected into a second stage inside the same gas cell, where systematically varying the injection delay enhances the injected bunch energy to 2.5 GeV and boosts background trapped electrons to 3 GeV, while reducing energy spread and preserving charge. These findings underscore the critical role of synchronization and plasma tailoring strategies relevant for future multi-pulse and flying-focus LWFA configurations.

LWFA are attractive acceleration techniques for generating electron beams with a broad range of energies, ranging from sub- GeV to $10\,GeV$, and potentially up to $100\,GeV$, on a compact scale, because of their substantial acceleration gradient on the order of tens to hundreds of GV/m[1–6]. Considerable advancement has been achieved in LWFAs during the past few decades, enabling the production of multi-GeV high-energy electron beams[7–9] together with high-quality, monoenergetic, high-brightness, and low-emittance e-beams[10–12] which open various applications in gamma-ray sources, free electron lasers, coherent x-ray sources and THz radiation generation[13–19].

An ultra-intense laser pulse ($I_0 > 10^{18}\ w/cm^2$), propagating through a gaseous target drives a plasma wakefield via the ponderomotive force. Electrons are expelled from the high-intensity region, leaving behind a near electron-free cavity. The stationary ions form a positively charged region that sustains a strong electric field directed toward the bubble center[20]. For effective acceleration, the displaced electrons must enter the accelerating phase of the bubble at the suitable location and velocity, where they can be trapped and subsequently accelerated to high energies[12]. However, achieving maximum energy and high-quality electron beam in LWFA is complicated by three main constraints: laser diffraction, pump depletion, and electron dephasing[21–23]. Several different methods have been employed to overcome these limitations for high energy gain such as enhancing electron injection techniques[24,25], optimizing laser parameters[2,26] and designing different plasma density profiles[17,27], which led to more stable and efficient acceleration.

While these solutions have considerably enhanced single-stage LWFA, the quest to improve the energy gain of the accelerated beam and enhance the acceleration length remains a continuous struggle. The most promising strategy to address single stage LWFA's intrinsic limitations is MSLWFA, where the acceleration process is divided into multiple stages, employing a separate laser pulse and plasma profiles for each stage[9,28–30]. This setup can enhance the beam parameters (emittance, divergence, etc.,) making it a versatile and powerful tool for creating multi-GeV electron beams[9,31]. MSLWFA demonstrates its ability to surpass the single-stage LWFA limitations so it stands as a promising solution for future accelerator and radiation source development. Various researches confirm the feasibility of this technique, demonstrating notable energy enhancements and improved

[1]National Laboratory on High Power Laser and Physics, Shanghai Institute of Optics and Fine Mechanics, Chinese Academy of Sciences, Shanghai 201800, China. [2]Center of Materials Science and Optoelectronics Engineering, University of Chinese Academy of Sciences, Beijing, Beijing 100049, China. [3]Department of Physics, Iran University of Science and Technology, Narmak, Tehran, Iran. [4]ELI-ALPS, ELI-HU Non-Profit Ltd, Wolfgang Sandner utca 3, Szeged H- 6728, Hungary. ✉email: xiexl329@siom.ac.cn; lx62@siom.ac.cn

beam quality as addressed in both experimental and computational configurations. For instance, an energy gain of 0.8 GeV with an acceleration gradient of $187\ GV/m$ was achieved in the second stage of acceleration, as reported by Jian Sheng Liu et al.,[32]. Recent advancements in two stage LWFA technology have demonstrated high energy gain capabilities[33,34]. According to H.T. Kim. et al., employing a 30 fs, $1\ PW$ laser pulse, 3-GeV energy gain using $2.1 \times 10^{18}\ cm^{-3}$and $0.18 \times 10^{18}\ cm^{-3}$ optimal plasma densities, can be achieved in a $10\ mm$ acceleration stage[7]. Pathak V. B. emphasizes the advantages of all optical dual stage LWFA in achieving higher energy (10-GeV) electron beams with a total power of $0.6\ PW$, increasing energy three times beyond single-color LWFA performance at equivalent power[31]. Zhan. J. reported the accelerated electron beam in the second stage, demonstrated 0.8 GeV energy and $\sim 1.6\ pC$ charge while maintaining an energy spread below 3%, aligned greatly with multidimensional PIC simulations[33]. Despite these considerable advances, several issues in two-stage LWFA still needs to be addressed, particularly the injection of the electron beam from the first stage into the accelerating phase of the wakefield in the second stage to ensure efficient inter-stage coupling. Moreover, precise synchronization between the electron beam exiting the initial stage and the laser pulse driving the second stage is essential to maximize energy gain and preserve beam quality.

With these challenges in mind, this work investigates a two-stage LWFA configuration implemented within a single gas cell with two gas inlets featuring trapezoidal density profiles for each stage. Utilizing SMILEI (PIC)[35], simulations were performed in both axisymmetric (AM) with two azimuthal modes ($m = 0,\ 1$) and 2D geometries. This study explores the dynamics of an electron bunch accelerated in the first stage and its subsequent injection and coupling into the second-stage wakefield. Systematic variation of the injection delay (the longitudinal spacing between the electron bunch injected from the first stage and the laser pulse in the second stage) between the electron bunch and the second laser pulse reveals distinct influences on energy gain and charge separation between the background-trapped and injected electron bunch. The results demonstrated in this study establish a conceptual framework for multi-stage LWFA by investigating injection delay and laser-plasma synchronization in two-stage LWFA. This approach also offers the groundwork for future flying focus implementation utilizing multi-pulse scheme to improve energy gain and beam quality for compact high-brightness electron and light sources for ultrafast X-rays, medical accelerators, and high-energy physics.

Results and discussions

The conceptual framework for a two-stage LWFA process is shown in Fig. 1. To drive successive wakefield stages, two high power laser pulses (each with $a_0 = 7.7,\ w_0 = 20\mu\, m,\ \tau\ = 30\ fs,\ \ E = 30\ J,\ \lambda_0 = 800\ nm$ and $I_0 = 1.2 \times 10^{20}\ W/cm^2$) are propagated and tightly focused at $x = 635\ \mu\, m$ (in the first stage) and $x = 3420\mu\, m$ (in the second stage) inside the gas cell which has a variable length as shown in Fig. 1(a). The gas cell contains He gas with an initial neutral density of $3.5 \times 10^{18} cm^{-3}$, which yields an electron density of $7 \times 10^{18} cm^{-3}$ after full ionization (two electrons per atom, with ionization model employed in PIC, depicted in Fig. 1(b). The gas cell, designed with variable length to suit experimental needs, features two gas inlets that produce tailored gas density profiles (First stage: 600 $\mu\, m$ up ramp, 2200 $\mu\, m$ plateau, 600 $\mu\, m$ down ramp. Second stage: 20 $\mu\, m$ up-ramp, 2200 $\mu\, m$ plateau, 20 $\mu\, m$ down ramp) for each individual stage as shown in Fig. 1 (b) and inset (c). A zero-density region ($35\mu\, m$) is maintained at the start of the first stage to ensure that the laser maintains its initial intensity and temporal profile. The wakefield structures and corresponding energy

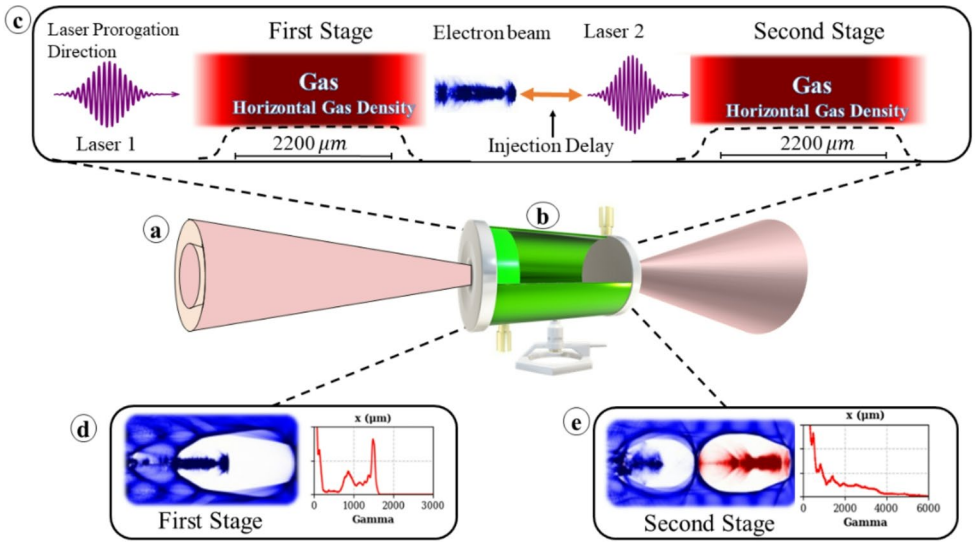

Fig. 1. A two-stage LWFA setup. (**a**) Two laser pulses are introduced and focused at different positions within a single gas cell to drive sequential Wakefield acceleration stages. (**b**) The gas cell contains helium gas with an electron density of 7×10^{18} cm^{-3} (after a full ionization with the laser pulses) (**c**) The density profile includes a uniform density region extending over 2200 $\mu\, m$ in both the stages. (**d**, **e**). The wakefield structures of both acceleration stages are also visualized.

spectra during the first and second stage LWFA are presented in Fig. 1 (d) and (e) respectively. In the first stage of acceleration, the laser pulse is focused at 635 $\mu\, m$, just beyond the end of the up ramp and at the edge of the plateau region. This positioning places the pulse within a stable, uniform plasma density, minimizing distortions caused by the density gradient in the up ramp and allowing the laser to maintain its intensity for longer duration of time during propagation along the plateau.

Building on the wakefield dynamics developed in the first stage, the density of electrons and the corresponding energy spectra at different times during the first stage (a1-a4, b1-b4) and second stage (c1-c4, d1-d4) LWFA is depicted in Fig. 2. At an early stage ($\tau\ = 1.6\, ps$), the laser having propagated $400\mu\, m$, nearly spherical shaped bubbles are formed with no trapped electrons because of the weak wakefield structure and low initial momentum of electrons to overcome the potential barrier for injection, as shown in Fig. 2 (a1). At this stage the laser pulse is still at the up-ramp region (which is $600\mu\, m$) having density lower (below injection threshold) than the peak density of the plasma. The energy spectrum shows no evidence of electron injection and acceleration at this stage as shown in Fig. 2(b1). At $\tau\ = 4.0\, ps$, after propagating nearly $1200\mu\, m$, the laser has entered the flat-top density region where the wake amplitude increases. A strong density spike appears at the rear of the first bubble, indicating self-injection, triggered when the wakefield amplitude exceeds the trapping threshold. This occurs because the phase velocity of the wake decreases slightly due to pump depletion and nonlinear elongation of the bubble, enabling background electrons to catch up and be trapped. The complete evacuation of electrons inside the bubble also signifies a transition into the nonlinear blowout regime as depicted in Fig. 2(a2). The corresponding energy spectrum in Fig. 2(b2) clearly shows that the electrons have already entered the acceleration phase.

In this blowout regime, the injected electron bunch remains positioned near the rear of the bubble, where the longitudinal electric field $//E_x//$ reaches its maximum. This favorable positioning enables electron bunch to gain energy efficiently over the $1200\, \mu\, m$ acceleration length since injection. At this stage $(\tau\ = 8.0\, ps)$, the laser has propagated nearly $2400\mu\, m$ and the observed bubble elongation in Fig. 2(a3) results from a combination of relativistic self-focusing of the laser and the nonlinear plasma response. Consequently, the spectrum in Fig. 2(b3) displays a narrow energy spread and high beam quality, indicative of well-phased acceleration in a stable wake. As the electrons gain energy approximately over $1900\mu\, m$ since injection, they approach the dephasing length, the point where they outrun the accelerating phase of the wakefield. This length, estimated by,

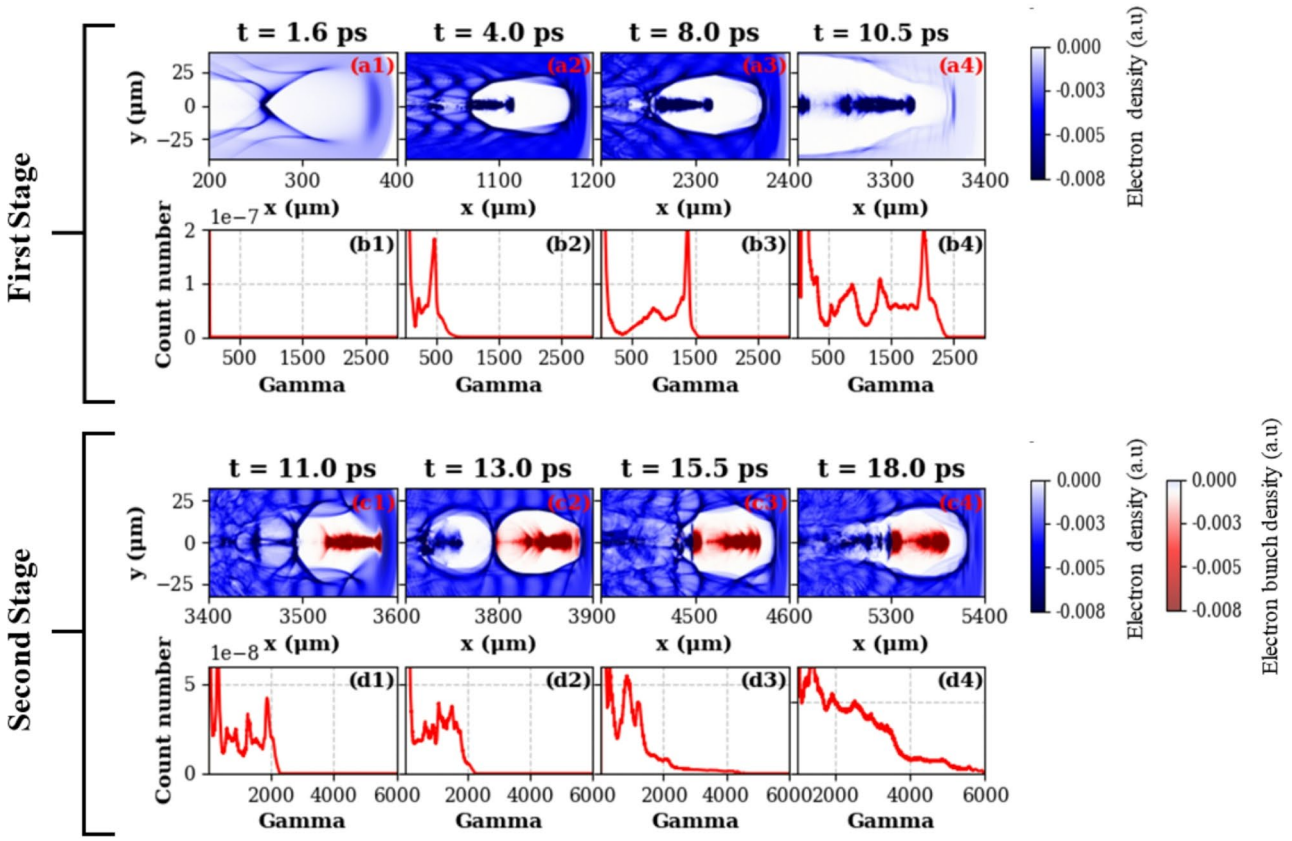

Fig. 2. First stage LWFA, electron density contours (top, a1-a4) and corresponding energy spectra (bottom, b1-b4) at times ($\tau\ = 1.6\, ps,\ 4.0\, ps,\ 8.0\, ps,$ and $10.5 ps$). Second stage LWFA, electron density contours (top, c1-c4) and corresponding energy spectra (bottom, d1-d4) at later times ($\tau\ = 11.0\, ps,\ 13.0\, ps,\ 15.5\, ps,\ 18.0\, ps$).

$$L_d = \lambda_p \left(\frac{n_c}{n_e} \right)^{1/2} = 1970\,\mu m$$

Where "$n_c \approx 10^{21}\,cm^{-3}$" is the critical density for $800\,nm$ laser and λ_p ($?12.6\,\mu m$) is the plasma wavelength. Furthermore, at this point ($\tau = 10.5\,ps$), the front of the electron bunch slips into the decelerating phase of the wake, as shown in Fig. 2(a4), while the rear of the bunch remains within the accelerating phase and continues to gain energy. This phase separation within the bunch, combined with the space charge of the electron bunch contributing to the wakefield, can cause elongation of the wake shape. Despite this complex and highly nonlinear evolution of the wakefield, the energy spectrum in Fig. 2(b4) exhibits a sharp, well-defined peak near $1\,GeV$ ($? 2000\,\gamma$) indicating monoenergetic beam. The relative stability of this spectral profile reflects reduced wakefield fluctuations during the main acceleration phase, which supports high beam quality and enables efficient coupling into the subsequent acceleration stage.

To achieve further acceleration, the electron beam from the first stage is extracted using tracked particle data and employed as input for the second stage. After a total propagation distance of $3400\mu\,m$ (2800 $\mu\,m$ since injection), the beam data are recorded without altering its divergence, emittance, or energy. These tracked particle data are then used to initialize the second-stage simulation. All beam characteristics, including momentum, energy, and spatial distribution, remain unchanged, ensuring that the second stage accurately represents the natural beam dynamics without artificial modifications and enabling a realistic study of two-stage acceleration. To maximize the energy gain, a second laser pulse with identical parameters and strength ($a_0 = 7.7,\ w_0 = 20\mu\,m,\ \tau = 30\,fs,\ E = 30\,J,\ \lambda_0 = 800\ nm$ and $I_0 = 1.2 \times 10^{20}\,W/cm^2$) is used to drive the injection of this $1\,GeV$ electron bunch. The laser is focused just beyond the up-ramp region at 3420 $\mu\,m$ within the second stage, which features a tailored density profile comprising a 20 $\mu\,m$ up-ramp followed by a 2200 $\mu\,m$ plateau. The spatial delay between the laser pulse and the electron bunch at this point is set to $2\lambda_p$. The resulting electron density contours and the corresponding energy spectra in the second stage LWFA are shown in Fig. 2 (c1-c4) and (d1-d4) respectively.

At the beginning of the second stage (at $\tau = 11.0\,ps$), the electron bunch, carrying its own space charge, modifies the plasma wakefield and enhances its amplitude. The increase in wakefield strength is localized around the bunch which enhance the trapping efficiency for electrons. However, because of the greater trapping threshold of the laser's self-focusing phase, background electrons are still un-trapped, and the density distribution shows no signs of injection as seen in Fig. 2(c1). Similarly, the energy spectrum in Fig. 2(d1) remains unchanged compared to the last timestep of the first stage, indicating that no electron trapping has occurred at this point in the second stage. However, as the laser pulse propagates deeper into the plateau region, the plasma density stabilizes and laser's self-focusing mechanism enhances the wakefield, making it more conducive to trapping. As a result, a distinct density spike emerges inside the second bubble (Fig. 2(c2)), signaling the onset of background electron trapping at $\tau = 13.0\,ps$. The injected electron bunch propagating further inside the wake and the background electrons gaining energy to reach $1.28\,GeV$ ($\gamma \approx 2500$) as depicted by the corresponding energy spectra Fig. 2(d2). The wakefield amplitude continues to enhance, as the electron bunch propagates deeper into the acceleration region. As illustrated in Fig. 2 (c2), the two bubbles, which were previously distinct and well-separated at $\tau = 13.0\,ps$, have now combined into a single, elongated bubble structure at $\tau = 15.5\,ps$, as shown in Fig. 2 (c3). This merging of bubbles is caused by the space-charge field effect and the propagation of laser pulse through the reduced plasma density gradient in the plateau region of the density profile, which causes the bubbles to overlap, merge into a single, lengthy structure. At this instance the laser pulse having propagated $4600\,\mu\,m$, drives a single elongated bubble, which produces a more stable and stronger wakefield, conducive to continued electron acceleration as clear in Fig. 2 (d3). At $\tau = 18.0\,ps$, the trapped electron reaches an energy of 3 GeV, while the electron bunch from the first stage carries an energy of 2.5 GeV. Notably, the spectrum of the trapped electrons exhibits a broad distribution, indicating efficient trapping across a wide range of energies. The absence of a distinct peak and broad (continuous) distribution is due the wakefield elongation driven by the increasing plasma wavelength "λ_p" due to the space charge effect. This leads to a non-uniform longitudinal electric field "E_x" across the electron bunch which flatten the wakefield locally, consequently the energy distribution becomes continuous rather than forming a quasi-monoenergetic peak. Since electrons, particularly those with lower energies are expelled out of the wakefield, lowering the quantity of high-energy particles. The low charge at $3\,GeV$, which is visible in the energy spectrum in Fig. 2 (d4), also indicates significant transverse expulsion driven by the radial field of the elongated bubble. Strategies such as density tapering or external focusing like plasma lenses can mitigate broad energy spread and help restore a more quasi-monoenergetic beam. Even with a broad energy spread, LWFA electron beams have important applications, including photon science and high-energy physics[36], radiotherapy[37] and high-resolution imaging and time-resolved studies[38].

To investigate and maximize the energy gain, the parametric 2D scan of injection delays ranging from $-2\lambda_p$ to $8\,\lambda_p$, where $\lambda_p = 12.63\ \mu\,m$, is conducted, and the resulting energy spectra of the background electrons is presented in Fig. 3 (a). It is evident that the highest energy is obtained from the $2\lambda_p$ injection delay as depicted in Fig. 3(a) (dashed blue line), with a spectrum that extends up to ~ 1.8 GeV energy with $0.01\,a.u.$ charge, while the injected bunch having entered the wakefield at the optimal phase, loses charge and reaches $0.00004\,a.u.$ as depicted in Fig. 3(b). The charge loss occurs because the bunch is not fully trapped in the wakefield. Instead, it primarily contributes to strengthening the wake by partly loading it, which efficiently traps and accelerates the background electrons. The strong transverse fields at this delay result in a high angular divergence (~ ± 55 mrad) as shown in Fig. 4. The strong wakefield scatters low-energy electrons more, causing them to spread outward, broaden the energy spread. Furthermore, reducing the injection delay to $-2\lambda_p$, the injected electron bunch is placed in front of the laser, prevents the wakefield from forming and lowers the longitudinal electric field "E_x"

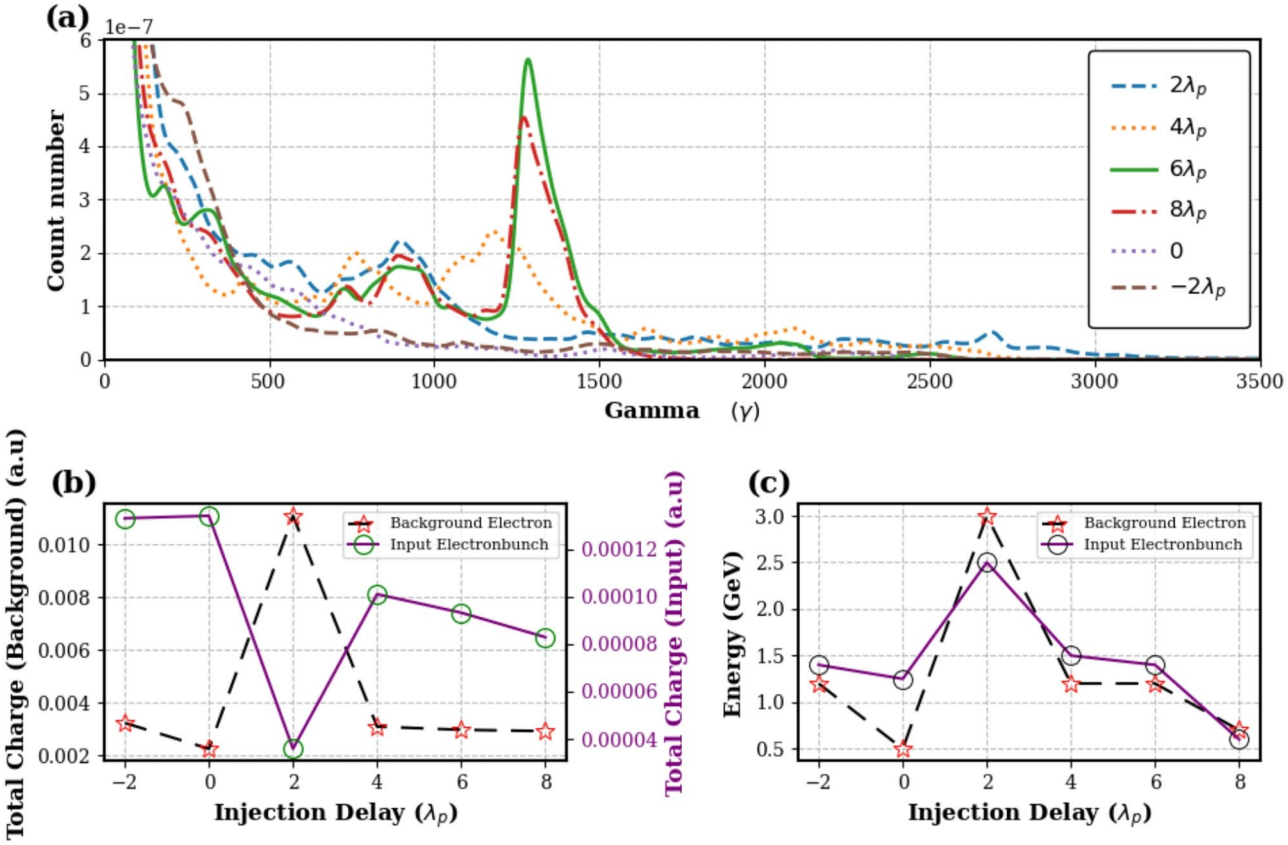

Fig. 3. **a**) Energy spectra of background electrons for different injection delays ($-2\lambda_p$ to $8\lambda_p$) 2D scan (**b**) Total charge of background electrons (black dashed line) and injected electron beam (purple solid line) versus injection delay. (**c**) Maximum energy of background electrons (black dashed line) and injected electron beam (purple solid line) versus injection delay.

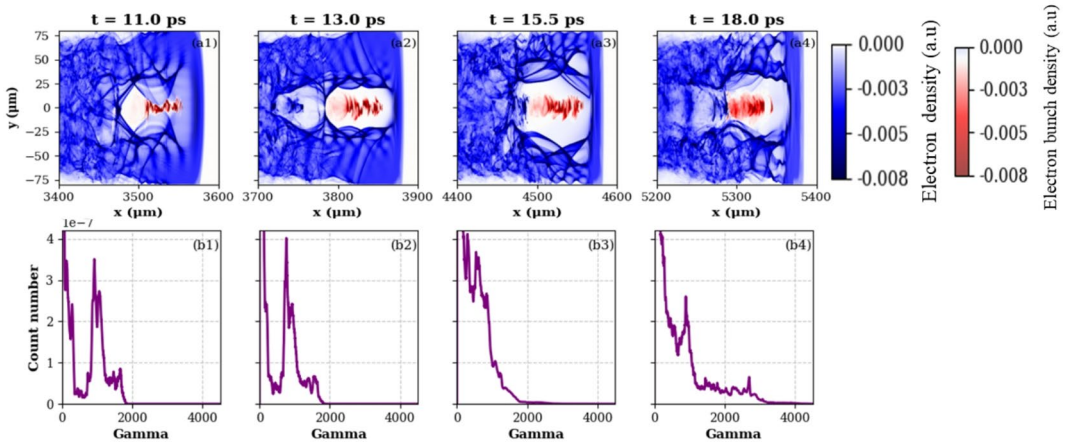

Fig. 4. Comparison of angular distribution (θ_y $(mrad)$) vs. Energy (GeV), considering first stage LWFA and different injection delays ($-2\lambda_p$ to $8\lambda_p$) during the second stage.

available for background electron acceleration. The wakefield amplitude receives suppression from the space charge buildup (~0.01 a.u.) within the bunch to create minimal background electron trapping, reducing the background electron charge to around 0.003 a.u., Fig. 3(b)) and resulting low energy gain from $\sim 0.2\,GeV$ to $\sim 1.2\,GeV$ along the propagation distance. Injecting the laser pulse and the electron bunch at the same time ($0\lambda_p$) (purple dotted line), the spectral width remained from ~0.2 GeV to 1 GeV. Although beam loading is still caused by the injected bunch overlap with the laser, some background electrons can be caught in the wakefield's

accelerating phase. The energy spread narrows compared to $-2\lambda_p$, indicating a more uniform longitudinal electric field "E_x" and more efficient acceleration, though the charge of the trapped background electrons remains lower than 0.003 a.u. and electron bunch higher than 0.01 (Fig. 3(b)). In contrast to the spectra at closer injection delays ($-2\lambda_p$, 0, and $2\lambda_p$), the energy spectrum of the background electrons at large injection delays of $4\lambda_p$, $6\lambda_p$ and $8\lambda_p$ shows clear peaks at $0.5\,GeV$, $0.6\,GeV$ and $0.6\,GeV$, with the maximum energy of $1.3\,GeV$, $1.2\,GeV$ and $1\,GeV$ respectively as shown is Fig. 3(a). The sharpness of these peaks, particularly at $6\lambda_p$ and $8\lambda_p$, indicates efficient trapping caused by optimal beam loading, which enables uniform acceleration of background electrons with a narrow energy spread. The angular divergence decreases to $\sim \pm 25\,mrad$ at these delays, reflecting less transverse scattering due to weaker transverse fields. At $6\lambda_p$ and $8\lambda_p$, the charge of the background electrons remains stable around 0.003 a.u., while the injected electron bunch maintains a charge of approximately 0.007 a.u. (Fig. 3(b)). This stability in charge indicates optimal beam loading, which efficiently accelerates the background electrons while minimizing transverse scattering. The lower angular divergence (~±25 mrad), shown in Fig. 4, further supports this observation. The total energy of background electrons and the injected electron beam plotted versus different injection delays, presented in Fig. 3(c), also summarizes the acceleration tendencies seen in the energy spectra by quantifying the maximum energy of the injected electron beam (purple solid line) and the background electrons (black dashed line) along the delay range of $-2\lambda_p$ to $8\lambda_p$ at last timestep of second stage acceleration. Moreover, Fig. 7 clarifies the energy spread as a function of injection delay. Optimal delays reduce the energy spread by improving the phase-space alignment of electrons with the wakefield, yielding a more monoenergetic beam. Shorter or non-optimal delays produce broader distributions due to less uniform acceleration.

To clarify the wakefield evolution, electron dynamics, and energy spectrum, the second-stage LWFA for the optimal injection delay of $2\lambda_p$ is investigated utilizing 2D Cartesian geometry, over $\tau = 11.0\,ps,\ 13.0\,ps,\ 15.5\,ps$, and $18.0\,ps$ as presented in Fig. 5. As depicted in Fig. 5(a1), the space charge field of electron beam increases the longitudinal electric field and enhances the Wakefield further. Since the injected electron beam has not yet had a major impact on background electron trapping, the energy spectrum maximum at this point peaks at $\sim 1.02\,GeV$ ($\gamma \approx 2000$), indicating the initial energy of the injected bunch with a tight spread, depicted in Fig. 5(b1). The trapped background electrons stay at significantly lower energies ($\gamma < 500$), whereas the majority of the high-energy electrons are part of the injected electron bunch as also verified in the combined energy spectra in Fig. 6 (a).

As the injected bunch has traveled ~ 700 $\mu\,m$ in the second stage, its space charge modifies the wakefield and set an environment to trap background electrons by slowing down the wake velocity.

The energy spectrum slightly shifts to the sharper side resulting the start of background electron acceleration in the second bubble as in Fig. 5(b2). The injection and acceleration at this stage is also clarified by Fig. 6 (b) (blue curve), shifting towards higher gamma values ($\gamma > 500$). But most of the high-energy electrons still belong to the injected electron bunch. At $\tau = 15.5\,ps$, the primary and secondary bubbles converge to form a single elongated bubble. By this point, the injected electron bunch has propagated approximately ~ 1400 $\mu\,m$, while the background electrons remain located at the rear of the elongated bubble, positioned in the accelerating phase of the wakefield, as evident in Fig. 5(a3). The corresponding energy spectra in Fig. 5(b3) reflects that the combined acceleration in the merged wakefield is a result of strong beam loading which modifies the wakefield

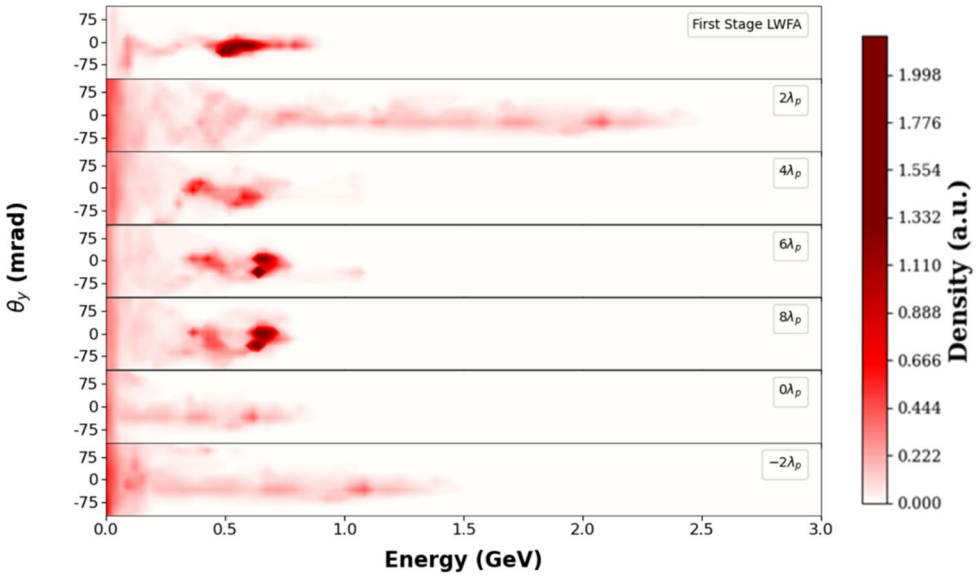

Fig. 5. Second stage LWFA (2D scan) at optimum injection delay of $2\lambda_p$, electrons density contours top (a1-a4) and corresponding energy spectra for background electrons bottom (b1-b4) at time $\tau = 11.0\,ps,\ 13.0\,ps,\ 15.5\,ps,\ and\ 18.0\,ps$..

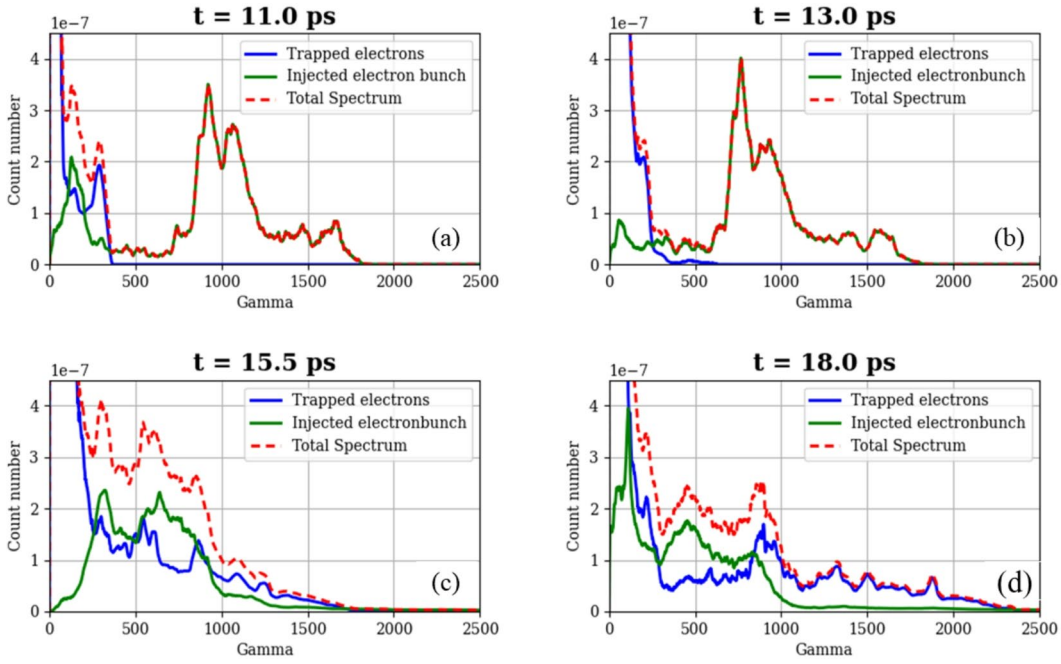

Fig. 6. The energy spectrum evolution for the optimal case $(2\lambda_p)$ at various instances of time ($\tau = 11.0\,ps$, $13.0\,ps$, $15.5\,ps$, and $18.0\,ps$) during the second stage LWFA for injected electron beam (green solid line), trapped background electrons (blue solid line) and the total energy spectrum (red dashed line).

and transverse dynamics broaden the distribution. At this instance, a notable contribution to the total spectrum is made by an extensive.

number of trapped electrons that have been accelerated to higher energies ($\gamma \sim 500 - 1500$) as shown in Fig. 6 (c).

The energy spread of the injected electron beam has also increased revealing that the phase mixing has started at this stage, where electrons inside the beam encounter somewhat different accelerating fields because of wakefield inhomogeneities. At this instance, more electrons gain energy beyond the originally injected electron bunch, which can be verified from the combined spectrum in Fig. 6 (c). At $18.0\,ps$, the laser pulse has propagated to approximately $\sim x = 5400\,\mu\,m$ with an increased electron density inside the wake, at the back of the injected electron bunch. At this point, the laser pulse is nearly depleted, and the wakefield has significantly weakened. Many of the injected electrons have reached the dephasing length and have entered the decelerating phase of the wakefield, as reflected by the reduced peak intensities and broader energy spread in the combined spectrum of the injected electron beam shown in Fig. 6 (d). Due to variations in the initial phase-space circumstances, the trapped electron population continues to shift to higher energies at the same time, albeit less effectively than the injected electron beam. Notably, the high-energy portion of the spectrum at this point becomes dominated by the trapped electrons rather than the injected bunch. This transition arises because the injected electrons, having lost synchronization with the accelerating phase due to dephasing, can no longer gain significant energy. In contrast, the trapped electrons being more effectively phase matched with the evolving wakefield still experience acceleration despite the weakened wakefield. Together, these effects constrain the maximum attainable energy and produce the intricate energy distribution observed in the final stage, as illustrated in Fig. 6 (d).

Simulation method

In order to better understand the physics of two-stage LWFA, we used the SMILEI code[35] to conduct series of PIC simulations using Azimuthal Mode (AM) geometry with two azimuthal modes ($m = 0, 1$) and 2D Cartesian geometry for the parametric scan of different simulation parameters. The AM geometry in Smilei is designed for simulations with cylindrical symmetry, where scalar and vector fields are decomposed into azimuthal modes. This reduces computational complexity by solving Maxwell's equations independently for each mode[39]. In AM geometry fields and current densities are calculated on a 2D grid, while macro-particles are tracked in 3D Cartesian space, with special boundary conditions applied at the axis to maintain numerical stability. In the first stage, a high intensity laser pulse (with $a_0 = 7.7$, $w_0 = 20\mu\,m$, $\tau = 30\,fs$, $E = 30\,J$ and $\lambda_0 = 800\ nm$) interacts with a gaseous He target having a tailored density profile. This profile includes a $600\mu\,m$ up-ramp, a $2200\mu\,m$ plateau, and a $600\mu\,m$ down-ramp, with an initial gas density of $3.5 \times 10^{18}\,cm^{-3}$.. Ionization is modeled self–consistently through tunnel ionization using the PPT–ADK formulation, which computes the ionization rate based on the species atomic number. This approach dynamically captures the successive ionization of He atoms during laser propagation, leading to the formation of a fully ionized plasma with a plateau electron density of $7 \times 10^{18}\,cm^{-3}$. The normalization procedure for length, time, and electric

field is based on standard SI units. The moving window scheme is employed, propagating at the group velocity ($v_{group} = 0.998\,c$) of the laser, having dimensions of $110\,\mu\,m$ and $80\,\mu\,m$ in the x and r directions respectively. In order to ensure adequate resolution for the interaction, the simulation domain is discretized into 6900×320 cells, with mesh resolutions $dx \approx 0.125$ and $dr \approx 2.0$ (normalized units), with 32 particles per cell. To ensure the stability and accuracy, the Courant–Friedrichs–Lewy (CFL) condition for the timestep (dt) is used, with $time\ step\ over\ CFL = 0.96$. For the second stage of acceleration, we use the track particle data obtained from the first stage to capture the electron beam that was accelerated in the initial plasma interaction. All characteristics of electron beam like momentum, energy and spatial distribution remain steady from the first stage to establish initial conditions for the following stages. Without altering these beam parameters, we ensure that the second stage realistically reflects the electron-beam's dynamics without any artificial changes. This enables us to investigate subsequent acceleration stage and energy gain in a more realistic manner. The simulation setup in the second stage remains the same as the first stage, except for the moving window size and gas density profile. The moving window size is changed to $190\mu\,m$ and $80\mu\,m$ in the x and r directions respectively, having 12000×320 cells in the longitudinal and transverse direction. The gas density profile in the second stage is modeled as $20\mu\,m$ up-ramp, $2200\mu\,m$ plateau, and $20\mu\,m$ down ramp with laser pulse focused at the edge of the plateau at $3420\mu\,m$ along the x-axis. Simulations were run until the laser pulse was nearly depleted, corresponding to a simulation time of $10.5\,ps$ ($t\_end = 10.5\,ps$) per stage. This duration captures the full acceleration process, including injection, acceleration, and dephasing effects. The total laser propagation distance across both stages is approximately $5440\mu\,m$ $(5.4\,mm)$ ..

Following the second acceleration stage, we conducted a 2D Cartesian scan to investigate the effects of the injection delay between the laser pulse in the second stage and the electron bunch injected from the first stage. For the simulation with 2D geometry, $150\,\mu\,m \times 80\,\mu\,m$ moving window is utilized, with 9400 and 320 cells in x and y direction, with 32 particles per cell.

In this work, both AM and 2D Cartesian geometries implemented in Smilei PIC code. While 2D Cartesian simulations confine fields and particles to a planar geometry (x, y), limiting their ability to capture three-dimensional effects, the AM approach decomposes electromagnetic fields into azimuthal harmonics on a 2D (x, r) grid and evolves particles fully in 3D Cartesian space (x, y, z). By including two azimuthal modes ($m = 0,\ 1$), the AM simulations capture both cylindrically symmetric and first-order asymmetric effects, such as laser polarization, asymmetric wake structures, and off-axis electron dynamics, which are absent or poorly represented in 2D Cartesian runs. Special boundary conditions on the cylinder axis ensure numerical stability and physical accuracy in AM simulations. Although AM simulations provide a significantly improved physical description, they are computationally more expensive than 2D Cartesian simulations. Therefore, for extensive parameter scans, the more affordable 2D geometry is used, while AM simulations are reserved for detailed studies requiring higher physical fidelity.

Summary and conclusions

A comprehensive multi-dimensional, open-source PIC simulation, employing both 2D Cartesian and azimuthal mode (AM) geometries with two modes $(m = 0,\ 1)$, was conducted using the SMILEI code to investigate two-stage LWFA. The 1 GeV electron beam generated in the first stage entered the second acceleration stage with a controlled injection delay relative to the second laser pulse, preserving its energy distribution and divergence for effective further acceleration. In the second stage, background electrons reached energies up to $3\,GeV$ ($\gamma \approx 5871$), while the injected bunch attained $2.5\,GeV$ ($\gamma \approx 4892$). This behavior, along with the combined spectrum, is illustrated in Fig. 2. A systematic 2D parametric study was performed for injection delays of $-2\lambda_p$, 0, $2\lambda_p$, $4\lambda_p$, $6\lambda_p$, and $8\lambda_p$. The analysis revealed strong modulation in the longitudinal electric field E_x, highlighting the roles of beam loading and transverse dynamics. Among the scanned values, an injection delay of $2\,\lambda_p$ i.e., a longitudinal spatial separation of $25\,\mu\,m$ between the driving laser pulse in the second stage and the injected electron bunch from the first stage, was identified as optimal. The $2\,\lambda_p$ delay resulted in a 3 GeV background electron beam (with a charge of $0.01\ a.u.$ and divergence of $\pm 55\,mrad$) and a 2.5 GeV injected electron bunch (with a charge of $0.003\ a.u.$). The charge loss in the injected bunch at $2\,\lambda_p$ is due to due to its large rms size and its partial trapping in the wakefield, while it also contributes to enhancing the wake, facilitating efficient acceleration of the background electrons. Closer injection timings, such as $-2\lambda_p$ and $0\lambda_p$, the energy distributions remained broader, with divergence of $\pm 35\,mrad$ and lower peak energies (~1.2 GeV for $-2\lambda_p$ and 0.5 GeV for $0\lambda_p$). The total charge for the background electrons at these delays was approximately $0.003\ a.u.$ and $0.002\ a.u.$, respectively. These delays still resulted in efficient electron trapping, but the wakefield was weaker, leading to lower energy gains. For longer delays, such as $6\lambda_p$and $8\lambda_p$, the beam quality improved, characterized by narrower energy spreads (as shown in Fig. 7) and stable charges around $0.01\ a.u.$, with a divergence of $\pm 25\,mrad$. However, despite the improved beam quality, the energy gain remained lower compared to $2\lambda_p$.

Initially high-energy components are dominated by the injected bunch, while background electrons appear in the lower energy range. As acceleration proceeds, more background electrons are trapped and gain energy, resulting in phase mixing that broadens the energy spectrum. Some injected electrons reach the dephasing length, causing a decline in their spectral peak, while background electrons continue to accelerate. The study concludes that a $2\lambda_p$ delay is an optimal condition for maximizing energy gain, while delays of $6\lambda_p$ and $8\lambda_p$ yield beams of higher quality, high charge and lower energy. These findings underscore the importance of two stage LWFA for high-energy beam generation, emphasizing the critical influence of injection delay on laser-beam coupling and energy optimization.

This study lays the foundational groundwork for future planned multi-stage LWFA experiments at Shanghai Institute of Optics and Fine Mechanics, Chinese Academy of Sciences, Shanghai (SIOM, CAS), utilizing Shenguang (SG-II) $5PW$laser facility. Using laser parameters of ($a_0 = 7.7,\ w_0 = 20\mu\,m,\ \tau = 30\,fs,$

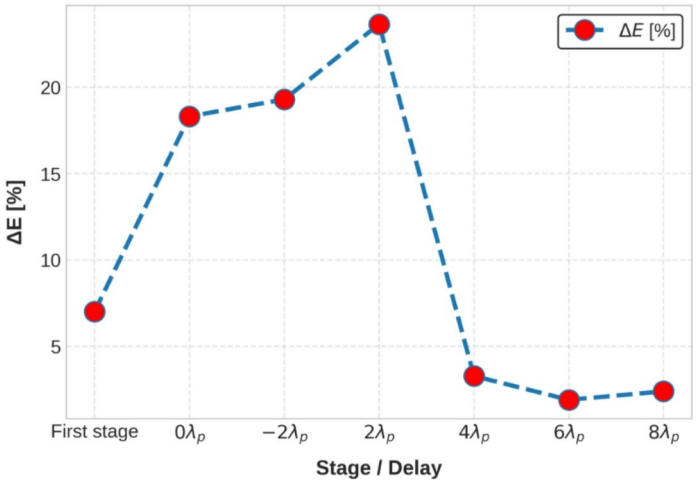

Fig. 7. Variation of the relative energy spread of the accelerated electron beam as a function of injection delay. The case with $2\lambda_p$ delay achieves the highest peak energy but exhibits the largest energy spread, indicating a trade-off between energy gain and beam quality.

$E = 30\ J$, $\lambda_0 = 800\ nm$ and $I_0 = 1.2 \times 10^{20}\ W/cm^2$), we aim to accelerate electron beams through three or more acceleration stages with tailored gas profile designs. The insights gained here regarding injection delay optimization and beam dynamics directly inform the design and operation of this upcoming experiment, enabling improved control over beam quality and energy gain. Moreover, this study lays the groundwork for future developments in multi-pulse LWFA and flying focus techniques, enabling spatiotemporal control for scalable multi-stage acceleration experiments.

Data availability

The data that support the findings of this study are available from the corresponding authors upon reasonable request.

Received: 30 May 2025; Accepted: 30 September 2025
Published online: 27 November 2025

References

1. Tajima, T. & Dawson, J. M. Laser electron accelerator. **Phys. Rev. Lett. 43**, 267. https://doi.org/10.1103/PhysRevLett.43.267 (1979).
2. Gonsalves, A. J. et al. Petawatt laser guiding and electron beam acceleration to 8 GeV in a laser-heated capillary discharge waveguide. *Phys. Rev. Lett.* **122**, 084801. https://doi.org/10.1103/PhysRevLett.122.084801 (2019).
3. Debus, A. et al. Circumventing the dephasing and depletion limits of laser-wakefield acceleration. *Phys. Rev. X.* **9**, 031044. https://doi.org/10.1103/PhysRevX.9.031044 (2019).
4. Shaw, J. L. et al. D. H. Froula. Path to a Single-Stage, 100-GeV electron beam via a Flying-Focus-Driven Laser-Plasma accelerator. arXiv:2505.00157 [physics.plasm-ph]. https://doi.org/10.48550/arXiv.2505.00157
5. Nakajima, K., Kim, H. T., Jeong, T. M. & Nam, C. H. Scaling and design of high-energy laser plasma electron acceleration high. *Power Laser Sci. Eng.* **3**, e10. https://doi.org/10.1017/hpl.2015.5 (2015).
6. Malka, V. et al. Principles and applications of compact laser–plasma accelerators. *Nat. Phys.* **4**, 447. https://doi.org/10.1038/nphys966 (2008).
7. Kim, H. T. et al. Multi-GeV laser Wakefield electron acceleration with PW lasers. *Appl. Sci.* **11** (13), 5831. https://doi.org/10.3390/APP11135831 (2021).
8. Qin, Z. et al. Multi-GeV cascaded laser Wakefield acceleration in a hybrid capillary discharge waveguide. *New J. Phys.* **24** (7), 073048. https://doi.org/10.1088/1367-2630/ac81e2 (2022).
9. Kim, H. T. et al. Enhancement of electron energy to the multi-GeV regime by a dual-stage laser-wakefield accelerator pumped by Petawatt laser pulses. *Phys. Rev. Lett.* **111** (16), 165002. https://doi.org/10.1103/PHYSREVLETT.111.165002 (2013).
10. Faure, J. et al. A laser–plasma accelerator producing monoenergetic electron beams. *Nature* **431**, 541–544. https://doi.org/10.1038/nature02963 (2004).
11. Geddes, C. et al. High-quality electron beams from a laser Wakefield accelerator using plasma-channel guiding. *Nature* **431**, 538–541. https://doi.org/10.1038/nature02900 (2004).
12. Mangles, S. et al. Monoenergetic beams of relativistic electrons from intense laser–plasma interactions. *Nature* **431**, 535–538. https://doi.org/10.1038/nature02939 (2004).
13. Kneip, S. et al. C., Bright spatially coherent synchrotron x-rays from a table-top source. *Nat. Phys.* **6**, 980. https://doi.org/10.1038/nphys1789 (2010).
14. Ta Phuoc, K. et al. All-optical Compton gamma-ray source Nat. *Photon* **6**, 308. https://doi.org/10.1038/nphoton.2012.82 (2012).
15. Corde, S. et al. E Femtosecond x rays from laser-plasma accelerators. *Rev. Mod. Phys.* **85**, 1. https://doi.org/10.1103/RevModPhys.85.1 (2013).
16. Albert, F. & Thomas A G R. Applications of laser wakefield accelerator-based light sources. *Plasma Phys. Control. Fusion* **58**, 103001. https://doi.org/10.1103/RevModPhys.85.1 (2016).
17. Kozlova, M. et al. Hard x rays from laser-wakefield accelerators in density tailored plasmas. *Phys. Rev. X.* **10**, 011061. https://doi.org/10.1103/PhysRevX.10.011061 (2020).

18. Wentao Wang, K. et al., Free-electron lasing at 27 nanometres based on a laser wakefield accelerator. *Nature* **595**, 516. https://doi.org/10.1038/s41586-021-03678-x (2021).
19. Mirzaie, M. R. P. M., Hojbota, C. I., Niknam, A. R., Massudi, R. & Kim, K. Y. Chang Hee Nam; investigation of Terahertz radiation generation from laser-wakefield acceleration. *AIP Adv.* **14** (2), 025347. https://doi.org/10.1063/5.0187339 (2024).
20. Esarey, E., Schroeder, C. B. & Leemans, W. P. Physics of laser-driven plasma-based electron accelerators. *Rev. Mod. Phys.* **81**, 1229. https://doi.org/10.1103/RevModPhys.81.1229 (2009).
21. Esarey, E. H., Shadwick, B. A., Schroeder, C. B. & Leemans, W. P. Nonlinear pump depletion and electron dephasing in laser Wakefield accelerators. **737**, 578–584. https://doi.org/10.1063/1.1842594 (2004).
22. Palastro, J. et al. Dephasingless laser Wakefield acceleration. *Phys. Rev. Lett.* **124** (13), 134802. https://doi.org/10.1103/PHYSREVLETT.124.134802 (2020).
23. Geddes, C. G. R. et al. Production of high-quality electron bunches by dephasing and beam loading in channeled and unchanneled laser plasma accelerators. *Phy Plasmas.* **12** (5), 056709. https://doi.org/10.1063/1.1882352 (2005).
24. Liu, S. et al. All-optical cascaded laser Wakefield accelerator using ionization-induced injection. *Phys. Rev. Lett.* **107**, 035001. https://doi.org/10.1103/PhysRevLett.107.035001 (2011).
25. Buck, A. et al. Shock-front injector for high-quality laser-plasma acceleration. *Phys. Rev. Lett.* **110** (185006). https://doi.org/10.1103/PhysRevLett.110.185006 (2013).
26. Wang, W. T. et al. High-brightness high-energy electron beams from a laser Wakefield accelerator via energy chirp control. *Phys. Rev. Lett.* **117**, 124801. https://doi.org/10.1103/PhysRevLett.117.124801 (2016).
27. Ke, L. T. et al. Xu. Near-GeV electron beams at a few per-mille level from a laser Wakefield accelerator via density-tailored plasma. *Phys. Rev. Lett.* **126** (214801). https://doi.org/10.1103/PhysRevLett.126.214801 (2021).
28. Kaganovich, D. et al. First demonstration of a staged all-optical laser Wakefield acceleration. *Phys. Plasmas.* **12** (10), 100702. https://doi.org/10.1063/1.2102727 (2005).
29. Foerster, F. M. et al. Stable and High-Quality electron beams from staged laser and plasma Wakefield accelerators. *Phys. Rev. X.* **12**, 041016. https://doi.org/10.1103/PhysRevX.12.041016 (2022).
30. Li, W. T. et al. Developments in laser Wakefield accelerators: from single-stage to two-stage. *Chin. Phys. B.* **24**, 015205. https://doi.org/10.1088/1674-1056/24/1/015205 (2015).
31. Pathak, V. B., Kim, H. T. & Vieira, J. Silva and Chang Hee Nam. All optical dual stage laser Wakefield acceleration driven by two-color laser pulses. *Sci. Rep.* **8**, 11772. https://doi.org/10.1038/s41598-018-30095-4 (2018).
32. Liu, J. S. et al. All-Optical cascaded laser Wakefield accelerator using Ionization-Induced injection. *Phys. Rev. Lett.* **107**, 035001. https://doi.org/10.1103/PhysRevLett.107.035001 (2011).
33. Zhan Jin, H. et al. Ryosuke Kodama. Coupling effects in multistage laser Wake-field acceleration of electrons. *Sci. Rep.* **9**, 20045. https://doi.org/10.1038/s41598-019-56654-x (2019).
34. Zhu, X., Z, Chen., M., Y, L. B., Liu. F, Ge, X. & L, Sheng, Z. M and Zhang. J. Electron relay acceleration in Wakefields driven by a single laser interacting with multi-stage plasma channels. *Phys. Plasmas.* **29**, 013101. https://doi.org/10.1063/5.0042090 (2022).
35. Derouillat, J. et al. SMILEI: a collaborative, open-source, multi-purpose particle-in-cell code for plasma simulation. *Comput. Phys. Commun.* **222**, 351–373. https://doi.org/10.1016/j.cpc.2017.09.024 (2018).
36. Yu, C. H. et al. Brilliant x-ray sources generation based on high-quality laser-driven Wakefield accelerator. **10811**, 1081105. (2018). https://doi.org/10.1117/12.2502000
37. Polanek, R. et al. 1 kHz laser accelerated electron beam feasible for radiotherapy uses: A PIC-Monte Carlo based study. *Nuclear Instruments Methods Phys. Res. Sect. A-Accelerators Spectrometers Detectors Assoc. Equip.* **987**, 164841. https://doi.org/10.1016/J.NIMA.2020.164841 (2021).
38. Gonzalez, I. G. Development and applications of a Laser-Wakefield X-ray source. (2018). https://lup.lub.lu.se/search/publication/42b213d4-d570-41e6-ab3e-67a2b1f7c5e0
39. Lifschitz, A. F. et al. Particle-in-Cell modelling of laser–plasma interaction using fourier decomposition. *J. Comput. Phys.* **228** (5), 1803–1814. https://doi.org/10.1016/j.jcp.2008.11.017 (2009).

Acknowledgements

This work was partially funded by the National Natural Science Foundation of China (NSFC) (12204500), the Key project of intergovernmental international scientific and technological innovation cooperation (2021YFE0116700) and CAS President's International Fellowship Initiative (grant no. 2025PVA0159). R. U. Haq is thankful to R. A. Nabi of SIOM, UCAS for his support and guidance. R. U. Haq gratefully acknowledges the Alliance of National and International Science Organizations (ANSO) Ph.D. fellowship for Young Talents.

Author contributions

X.L.X. and X.L. conceived the initial idea of two stage LWFA. R.U.H and M.R.P performed smilie PIC simulation and post processed data . R.U.H., M.R.P and G.L.Z. contributed in data visualization. P.Z. and M.S. revised the article draft. R.U.H. , L.Z , H.X and L.J.L analyzed and processed all the data. N.A.M.H. and J.Z supervised the project. All authors reviewed and contributed to the manuscript text.

Declarations

Competing interests

The authors declare no competing interests.

Additional information

Correspondence and requests for materials should be addressed to X.X. or X.L.